Chemical Science

ROYAL SOCIETY OF CHEMISTRY

EDGE ARTICLE

View Article Online
View Journal

Cite this: DOI: 10.1039/d5sc08521g

All publication charges for this article have been paid for by the Royal Society of Chemistry

Inch-sized achiral perovskite ferroelectric single crystals for multiaxial passive circularly polarized light response

Yueying Wang,†[a] Zeng-Kui Zhu,†*[a] Yuhang Jiang,[a] Jianbo Wu,[c] Wenhui Wu,[a] Haodong Ge,[a] Yong Wang,[b] Yao Li,[b] Huawei Yang,[a] Panpan Yu,*[a] Ying Zeng,[a] Song Yang*[d] and Junhua Luo *[ab]

In recent years, hybrid perovskite ferroelectrics with significant spontaneous polarization features have shown prominent advantages in passive circularly polarized light (CPL) detection. Nonetheless, the successful realization of multiaxial ferroelectric semiconductors for multidirectional CPL detection under zero bias remains a considerable challenge. Herein, a multiaxial passive CPL detector is achieved, benefiting from the bulk photovoltaic effect (BPVE) in an achiral biaxial ferroelectric $EA_4Pb_3Br_{10}$ (**1**, EA = ethylamine). In particular, achiral perovskite ferroelectric **1** crystallizes in a chiroptical-active polar point group (*mm*2) with excellent biaxial spontaneous polarization (P_s, 4.1 and 3.8 μC cm^{-2}) to multiaxial CPL response at zero bias. In detail, a clear image of the "H" letter was obtained along the *c*- and *a*-axes, respectively, demonstrating the favourable photoelectric performance of **1**. Notably, by leveraging its unique biaxial properties, the resulting device exhibits a distinct response difference of approximately 21% and 18% under right- and left-handed CPL excitation along two polar axes, comparable to many materials incorporating chiral components. It also shows excellent stability under the illumination of 405 nm CPL along both polar axes. This work represents a significant advancement in multidirectional photodetectors, highlighting the potential of multiaxial ferroelectric materials.

Received 3rd November 2025
Accepted 3rd April 2026

DOI: 10.1039/d5sc08521g

rsc.li/chemical-science

Introduction

The rapid progress in optoelectronic technologies has driven significant interest in materials capable of detecting circularly polarized light (CPL), a feature essential for applications such as satellite communication, remote sensing, quantum computing, and information storage.[1–4] Conventional CPL photodetector (CPL-PD) materials are mainly inorganic semiconductors, such as Si, InGaAs, *etc*. But due to the lack of inherent chirality, they have to rely on a linear polarizer and a quarter-wave plate. This strategy will hinder the device integration and miniaturization to some extent. In recent years, organic–inorganic hybrid perovskites (OIHPs) have gained much attention due to their remarkable optoelectronic properties, including adjustable bandgaps, high absorption coefficients, and superior carrier mobility-lifetime ($\mu\tau$) product.[5–8] For instance, Wu *et al.* proposed a 3D CPL-PD utilizing (*R*-PyEA)Pb_2Br_6 (*R*-PyEA = (*R*)-1-(pyridine-4-yl)ethan-1-amine), which exhibits obvious CPL distinguishability of 42% at 5 V.[9] The reported materials [(*R*)-3APr]PbI_4 ((*R*)-3APr = (*R*)-3-aminopyrrolidine) shows excellent CPL distinguishing ability with photocurrent anisotropy factors of 65% at 10 V.[10] In fact, chiral components are not essential for achieving CPL responses, as achiral crystals belonging to four asymmetric point groups (*m*, *mm*2, 4, and 42*m*) can also exhibit similar behavior,[11–14] such as (4-AMP)BiI_5 (4-AMP = 4-(aminomethyl)piperidinium) and $(IBA)_2(EA)_2Pb_3I_{10}$ (IBA = 4-isopropylbenzylammonium, EA = ethylammonium).[15,16] It is meaningful and crucial to continue enriching this type of materials to achieve direct and highly efficient CPL response in achiral systems.

Achiral OIHP ferroelectrics crystallizing in chiroptical-active polar point groups are very suitable for passive CPL detection. The built-in electric field allows passive detection, energy efficiency, and transportability. The chiroptical-active benefit permits CPL response without chiral ligands. Recently, achiral ferroelectric-based PDs have shown excellent CPL detection

[a]*College of Chemistry and Materials, School of Chemical Engineering, Key Laboratory of Fluorine and Silicon for Energy Materials and Chemistry of Ministry of Education, Jiangxi Province Key Laboratory of Porous Functional Materials, Jiangxi Normal University, Nanchang, Jiangxi 330022, China. E-mail: zkzhu@jxnu.edu.cn; ppyu@jxnu.edu.cn*

[b]*State Key Laboratory of Functional Crystals and Devices, Fujian Institute of Research on the Structure of Matter, Chinese Academy of Sciences, Fuzhou, Fujian 350002, China. E-mail: jhluo@fjirsm.ac.cn*

[c]*Department of Materials Science and Engineering, City University of Hong Kong, Kowloon, Hong Kong SAR 999077, China*

[d]*Jiangxi Provincial Key Laboratory of Advanced Electronic Materials and Devices, Jiangxi Science and Technology Normal University, Nanchang, 330038, China. E-mail: yangsong1230@126.com*

† Y. Wang and Z.-K. Zhu contributed equally to this work.

performance, *e.g.* $(CPA)_2FAPb_2Br_7$ (CPA = chloropropylammonium, FA = formamidinium) and $(n\text{-HA})_2CsPb_2Br_7$ (n-HA = n-heptanamine).[17,18] However, these devices can only be fabricated along the single polar crystallographic axis direction. This limitation inherently results in the reported passive CPL-PDs being uniaxial, thereby increasing the cost and complexity associated with device fabrication. This primarily originates from the intrinsic crystal symmetry and polarization distribution characteristics of these materials.[19,20] Comparatively, multiaxial ferroelectrics can exhibit photoresponses along different crystallographic axes, which helps to simplify optical systems to a certain extent. Since there is a great blank in multi-axis CPL detection, it's both imperative and challenging to explore multiaxial ferroelectric materials capable of highly CPL-sensitive detection.

Herein, a multiaxial passive CPL-PD is achieved utilizing an inch-sized reported ferroelectric $EA_4Pb_3Br_{10}$ (**1**, EA = ethylamine). **1** exhibits direct piezoelectric coefficients (d_{33}) of 11.5 and 11.8 pC N^{-1} along the *c*- and *a*-axes, respectively, comparable to the values reported by Wang *et al.*[21] and confirming its non-centrosymmetric polar crystal structure. Crystallizing in an optically active yet achiral polar point group (*mm*2) and showing obvious ferroelectric properties with P_s values of 4.1 and 3.8 μC cm^{-2} lay a foundation for CPL detection at zero bias. At 405 nm, a clear image of the "H" letter was obtained along each of the two polar axes, showing favorable photoelectric properties of **1**. Notably, benefiting from its uniquely biaxial properties, the **1′** PD shows high CPL-sensitive detection performance along both the *c*- and *a*-axes. The asymmetric factors reach up to 21% and 18% along the above axes, on par with most typical chiral components. Additionally, **1** also demonstrates exceptional stability under the illumination of 405 nm CPL along both polar axes. This work significantly promotes the application of multiaxial ferroelectrics in the field of multiaxial CPL detection, providing ideas for the development of multifunctional photoelectric detection materials.

Results and discussion

By reacting stoichiometric amounts of EA and $Pb(Ac)_2 \cdot 3H_2O$ in hydrobromic acid (HBr), the reported lead-halide ferroelectric $EA_4Pb_3Br_{10}$ (**1**) was successfully synthesized.[22] As shown in Fig. 1a and S1 (SI), **1** adopts a 2D trilayered perovskite structure templated by the simple EA cation and exhibits similar symmetry along the *a*- and *c*-axes, thus leading to similar atomic arrangements and bonding environments along these axes. A yellow, inch-sized single crystal (SC) with dimensions up to 52 × 4 × 2 mm^3 was facilely obtained *via* a cooling procedure (Fig. S2, SI). The purity of **1** is confirmed by powder X-ray diffraction (PXRD) analysis (Fig. S3, SI). As depicted in Fig. S4 (SI), thermogravimetric analysis reveals the ultrahigh thermal stability of **1** up to 550 K. Subsequently, XRD scans of the bulk SC surface exhibit strong and sharp (0 k 0) peaks, indicating a high degree of crystal orientation (Fig. S5, SI). Additionally, the flat and smooth (0 k 0) planes are evident in both the scanning electron microscopy (SEM) image (Fig. S6, SI) and atomic force microscopy (AFM) image (Fig. S7, SI), further confirming the excellent crystal quality of **1** (*i.e.*, a root-mean-square roughness of 0.054 nm).[23] Thus, we have successfully synthesized high-quality, large-size SC **1**, which lays a foundation for achieving superior photodetection performance.

At the ferroelectric phase (FEP), **1** crystallizes in the orthorhombic *C*2*cb* with *mm*2 point group (CCDC number: 1917092). There is a pair of spiral optical axes related by mirror symmetry within this crystal: along one of the spiral optical axes, the crystal lattice shows the characteristics of left-handed spiral arrangement; along the other spiral optical axis obtained by mirror symmetry, the lattice shows the characteristics of a right-handed spiral (Fig. S8 (SI)).[24,25] What's more, **1** can exhibit significant piezoelectricity.[26] Firstly, the crystal orientation is obtained in Fig. S9 (SI). Then, as shown in Fig. 1b and S10 (SI), significant piezoelectric response along the two polar axes endows **1** direct piezoelectric coefficient (d_{33}) of 11.5 and 11.8 pC N^{-1}, respectively, confirming its non-centrosymmetric polar crystal structure capable of generating charges in response to mechanical forces. In contrast, **1** adopts the centrosymmetric space group *I*4/*mmm* (CCDC number: 1880495) at the paraelectric phase (PEP). The lattice parameter relationship between the PEP and the FEP is $a^{FEP} \approx a^{PEP} + b^{PEP}$, $b^{FEP} \approx c^{PEP}$, $c^{FEP} \approx a^{PEP} - b^{PEP}$ (Fig. S11a, SI). The *ab*-plane of the PEP corresponds to the *ac*-plane of the FEP. As illustrated in Fig. 1c, this structural phase transition is accompanied by symmetry breaking, which is denoted by the Aizu notation 4/*mmm* → *mm*2. This transition is classified among the 88 types of ferroelectric phase transitions.[27] Notably, the number of symmetry elements reduces from 16 (E, $2C_4$, $5C_2$, i, $2S_4$, σ_h, $2\sigma_v$, $2\sigma_d$) to 4 (E, C_2, $2\sigma_v$). This reduction implies that there are four equivalent polarization directions ($r = 16/4$) in the FEP (Fig. S11b, SI), confirming that **1** exhibits biaxial ferroelectricity.[22,28,29] Furthermore, ferroelectric tests along polar axial directions (Fig. 1d) reveal rectangular polarized electric field (*P*–*E*) hysteresis loops along the *c*- and *a*-axes. The P_s values of 4.1 and 3.8 μC cm^{-2} are approximately equal to the reported ones (~3.5 μC cm^{-2}),[22] larger than other multiaxial ferroelectrics, such as $(n\text{-HA})_2CsPb_2Br_7$ (~1.6 μC cm^{-2}), (*R*)-(−)-3-hydroxlyquinuclidinium (~2.4 μC cm^{-2}), and $[(CH_3)_3NOH]_2[KFe(CN)_6]$ (~0.58 μC cm^{-2}).[18,30,31] This also indicates that P_s can be achieved along both the *c*- and *a*-axes. All these results expose that **1** is a biaxial ferroelectric material, potentially enabling biaxial passive photodetection.

Then, the **1′** semiconductor performance was analyzed. The UV-vis absorption exhibits an optical absorption cutoff edge at 451 nm, with an estimated bandgap of 2.77 eV (Fig. S12, inset, SI), indicating its optical absorption characteristics. In Fig. S13 (SI), the projected density of state (PDOS) shows that the Pb-5p and Br-4p orbitals of the inorganic perovskite backbone are the major contributors to the bandgap. Considering its absorption edge of 451 nm, **1** can only absorb light with wavelengths below this limit. Moreover, **1** adopts the polar space group *C*2*cb* at the FEP, which belongs to the *mm*2 chiroptical-active point group (Fig. S14, SI). The noncentrosymmetric stacking structure is responsible for chiroptical-active signals, which facilitate CPL detection at 405 nm.[15]

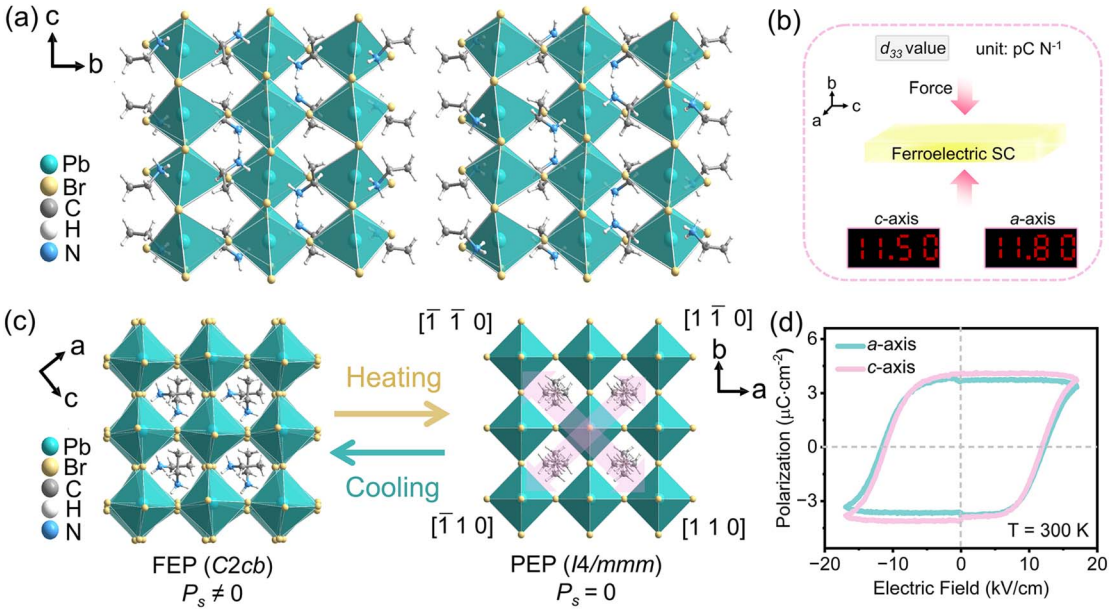

Fig. 1 (a) Crystal structure of **1** at room temperature; (b) the piezoelectric properties of **1** along polar axes; (c) comparison of building blocks for inorganic frameworks at FEP (left) and PEP (right), respectively; (d) polarization electric field hysteresis loops of **1** along polar axes.

The significant biaxial spontaneous polarization and inherent semiconductor performance are beneficial to its passive photoelectric response. Fig. S15 (SI) demonstrates that the device constructed along the polar axes exhibits significant bulk photovoltaic effects (BPVE) with a photovoltage of 0.5 V after polarization treatment under 405 nm illumination. This photovoltage can act as a driving force to enhance the separation and transport of charge carriers, thereby enabling the PD device to perform passive photodetection efficiently. What's more, a large carrier mobility-lifetime ($\mu\tau$) product further ensures high photocurrent for PDs and can be derived by fitting the measured photocurrent according to the Hecht equation $I = \frac{I_0 \mu\tau V}{L^2}\left[1 - \exp\left(-\frac{L^2}{\mu\tau V}\right)\right]$,[32] I, I_0, V, and L represent the photocurrent, the saturated photocurrent, external bias, and thickness, respectively. As shown in Fig. S16 (SI), the $\mu\tau$ values of **1** along two polar axes reach up to 7.63×10^{-4} and 6.01×10^{-4} cm^{-2} V^{-1}, respectively, comparable to the reported ones and that of state-of-the-art 2D perovskite-based photodetectors,[21,33] demonstrating the excellent carrier transport capability of polar biaxial ferroelectric **1**. Furthermore, **1′** optoelectronic imaging performance was also explored and shown in Fig. 2a and S17 (SI).[34–36] The incident beam at 405 nm is adjusted to maintain a 1 mm spot diameter, ensuring fully within the 2 mm^2 sensing area of the SC detector. A hollow metal mask engraved with the letter "H" is positioned between the light source and the SC-based device as the imaging target. Controlled by a stepper motor with a 1 mm step size, the mask allows precise movement along the *x*- and *y*-axes. This optical arrangement permits the laser beam to pass through the patterned mask before reaching the photodetector. To provide a visual reference, a 5 mm scale bar is included in Fig. 2b. During data collection, photocurrent is exclusively measured in the crystal regions illuminated through the mask apertures, while non-illuminated areas show only dark current. By recording the photocurrent response at each discrete position during raster scanning, the dataset is transformed into a patterned image using a 10 × 10 matrix conversion, thus achieving superior photoelectric imaging performance.[37] Fig. 2b illustrates the successful acquisition of a "H"-shaped image with clear outlines and distinct boundaries along the two polar axes. Additionally, the photocurrents along the *a*-axis and *c*-axis are comparable in magnitude. Fig. 2c shows the *I*–*t* curves along the *x*-axis and *y*-axis during imaging. Such results demonstrate the good photoelectric performance of our SC-based device. Meanwhile, benefiting from a stable BPVE drive, the photocurrent shows negligible change under long exposure and multiple on/off cycles (Fig. S18, SI), showing its excellent durability in passive photoelectric detection. Strong BPVE, large $\mu\tau$, and stable photoresponsive behavior suggest its application potential in the field of high-performance passive CPL detection.

Before formal testing, the incident light's polarization state was rigorously calibrated. Detailed schematic diagrams of the optical setup (Fig. S19 and S20, SI) and a corresponding table (Table S1, SI) were presented to confirm the power stability and guarantee the reliability of subsequent results (Fig. S21, SI). Then, the CPL photodetection based on **1** has been investigated at zero bias (Fig. 3a). Despite the *mm*2 point group is nonchiral, it's clearly identified as one of the optically active point groups.[38] Its optical behavior shows notable directional reliance, not exhibiting chirality on a macroscopic scale, yet it can exhibit optical activity in specific directions.[39] Thus, the CPL was controlled using a polarizer and a rotating 1/4 waveplate, with incidence along one of the two optical axes corresponding to the *mm*2 point group (Fig. S22, SI).[15,17] Furthermore, by

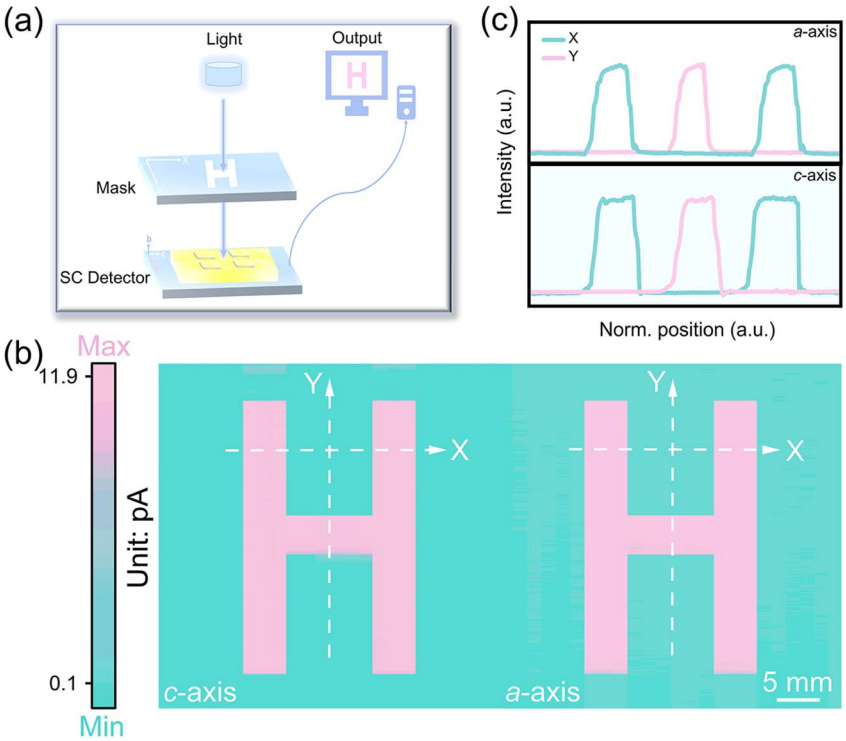

Fig. 2 (a) Schematic diagram of imaging device; (b) the image under 405 nm illumination with a power density of 75.4 mW cm^{-2}. A scale bar: 5 mm; (c) the normalized photocurrent signal intensity curves obtained from the imaging measurements correspond to the location indicated by the white dashed line in (b).

rotating the angle of the 1/4 waveplate from 0° to 360°, distinct differences in photocurrents are observed between right-hand circularly polarized light (RCP) and left-hand circularly polarized light (LCP) sources. As depicted in Fig. 3b, the passive photocurrent varies periodically with the circular polarization angle and demonstrates the ability to distinguish between RCP

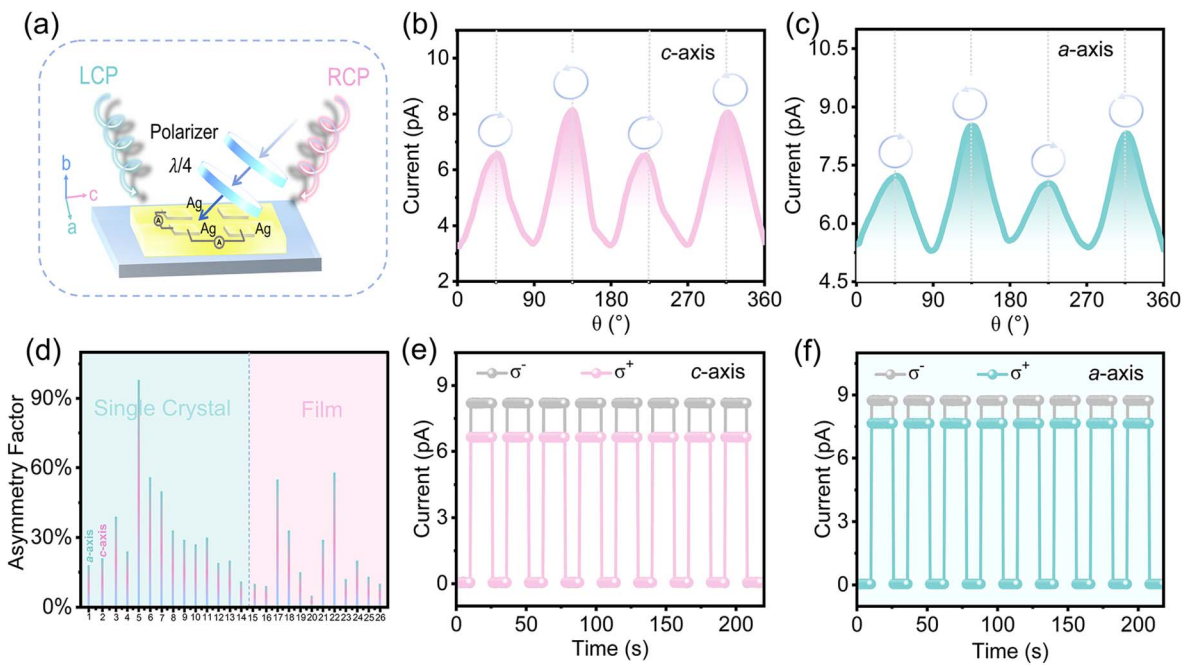

Fig. 3 (a) Schematic illustration of the CPL-PD; (b and c) angle-dependent photocurrent of **1** measured at 0 V bias at 405 nm (75.4 mW cm^{-2}); (d) comparison of the experimental asymmetry factor of **1** with other CPL detectors (see Table S2); (e and f) recyclable switching operation of the photocurrent under left (σ^-) and right (σ^+) CPL.

and LCP. To quantify this sensitivity to CPL, the asymmetry factor (g_{Iph}) was calculated using the formula, $g_{Iph} = 2(I_L - I_R)/(I_L + I_R)$,[40] I_L and I_R are the photocurrents under LCP and RCP illumination, respectively. The g_{Iph} is calculated to be 21% along the *c*-axis. Such a result may be attributed to the angular carrier drift arising from the spin-dependent BPVE in the ferroelectrics and provides more options for future CPL-PD materials.[17,41] In addition, it would also have the capability along the *a*-axis with a responsiveness asymmetry factor of 18% (Fig. 3c). Whether along the *c*- or *a*-axes, the g_{Iph} values are both in the range of previously reported 2D hybrid perovskites that introduce chiral cations as exampled by $[(R)$-β-MPA$]_2$MAPb$_2$I$_7$ (MPA = methylphenethylamine, 20% @ 532 nm), *S*-[(4-aminophenyl) ethylamine]$_2$AgBiI$_8\cdot$0.5H$_2$O (27% @ 520 nm), and *R*-(BrBA)$_2$PbBr$_4$ (11% @ 405 nm),[33,42,43] *etc.* (Fig. 3d, Table S2, SI). It's worth mentioning that there is no obvious attenuation after multiple cycles along both the *c*- and *a*-axes (Fig. 3e and f), indicating that **1** has excellent stability. Furthermore, to confirm the distinct directional optical behavior of *mm*2 point group crystals, a classic two-dimensional single-layer perovskite, *n*-BA$_2$PbBr$_4$ (*n*-BA = *n*-butylamine, CCDC 1945905) with a symmetrical central structure (Fig. S23a, SI), was chosen for comparison.[44] Its optical response was tested under identical experimental conditions (*i.e.*, under the same LCP and RCP irradiation), as depicted in Fig. S23b (SI). It distinctly reveals that the *n*-BA$_2$PbBr$_4$ crystal is unable to differentiate between RCP and LCP. This underscores the directional reliance of the optical behavior of *mm*2 point group crystals. These experimental results are of great significance for the selection of a new ferroelectric semiconductor for multiaxial PDs.

Conclusions

In summary, we selected and synthesized the inch-size (52 × 4 × 2 mm^3) single crystal EA$_4$Pb$_3$Br$_{10}$ (**1**). **1** has excellent biaxial spontaneous polarization of 4.1 and 3.8 μC cm^{-2} and good semiconductor properties. The stable and clear photoelectric imaging capability along the *c*- and *a*-axes, respectively, is also shown at 405 nm. Additionally, based on its biaxial ferroelectric property and crystallizing in the *mm*2 chiroptical-active point group, **1** achieves passive CPL detection of asymmetry factors of 21% and 18% along the *c*- and *a*-axes, respectively, with excellent stability. Such two values are on par with many materials that introduce chiral cations for CPL detection. This work shows that biaxial passive CPL detection is successfully realized by chiroptical-active point groups and spontaneous polarization of multiaxial ferroelectricity.

Author contributions

Y. Wang, and Z.-K. Zhu contributed equally to this work. Y. Wang prepared the samples. Y. Wang and Z.-K. Zhu wrote the manuscript. Y. Jiang, W. Wu, H. Ge, and H. Yang performed the photoelectric properties. J. Wu, Y. Wang, and Y. Li provided suggestions for the project. Z.-K. Zhu, P. Yu, Y. Zeng, S. Yang, and J. Luo designed and directed this project.

Conflicts of interest

There are no conflicts to declare.

Data availability

The data that support the findings of this study are available on request from the corresponding authors, [Zeng-Kui Zhu] and [Junhua Luo], upon reasonable request.

Supplementary information (SI) is available. See DOI: https://doi.org/10.1039/d5sc08521g.

Acknowledgements

This work was financially supported by the National Natural Science Foundation of China (22435005, 22193042, 22201284, 22305105, 22405108 and 22501112), the Natural Science Foundation of Fujian Province (2023J05076), the Jiangxi Provincial Natural Science Foundation (20252BAC200222, 20242BAB25129, 20232BAB213020), the Graduate Innovation Fund Project of Jiangxi Provincial Department of Education (YJS2025012).

Notes and references

1 Y. Liu and P. Xing, *Adv. Mater.*, 2023, **35**, 2300968.
2 E. Togan, Y. Chu, A. S. Trifonov, L. Jiang, J. Maze, L. Childress, M. V. G. Dutt, A. S. Sørensen, P. R. Hemmer, A. S. Zibrov and M. D. Lukin, *Nature*, 2010, **466**, 730–734.
3 A. Ishii and T. Miyasaka, *Sci. Adv.*, 2020, **6**, eabd3274.
4 A. Pietropaolo, A. Mattoni, G. Pica, M. Fortino, G. Schifino and G. Grancini, *Chem*, 2022, **8**, 1231–1253.
5 Z. Yang, Y. Bai, J. Yao, J. Wu, S. Cao, Y. Qiu, B. Zou, M. Yuan, J. Xu, L. Wan and R. Zeng, *Nano Res.*, 2025, **18**, 94907554.
6 H. Lu, Z. V. Vardeny and M. C. Beard, *Nat. Rev. Chem.*, 2022, **6**, 470–485.
7 Y. Dang, X. Liu, B. Cao and X. Tao, *Matter*, 2021, **4**, 794–820.
8 Y. Liu, X. Zhang, X. Xu, J. Dai and Z. Quan, *Angew. Chem., Int. Ed.*, 2025, e202510579.
9 J. Bai, H. Wang, J. Ma, Y. Zhao, H. Lu, Y. Zhang, S. Gull, T. Qiao, W. Qin, Y. Chen, L. Jiang, G. Long and Y. Wu, *J. Am. Chem. Soc.*, 2024, **146**, 18771–18780.
10 L. Wang, W. Hao, B. Peng, J. Ren and H. Li, *Adv. Mater.*, 2025, **37**, 2414199.
11 H. Li, F. Song, D. Zhu, Y. Song, C. Zhou, F. Ke, L. Lu, X. Kang and M. Zhu, *J. Am. Chem. Soc.*, 2022, **144**, 4845–4852.
12 B. Kahr, A. T. Martin and K. H. Ernst, *Chirality*, 2018, **30**, 378–382.
13 J. Zhao, T. Zhang, X.-Y. Dong, M.-E. Sun, C. Zhang, X. Li, Y. S. Zhao and S.-Q. Zang, *J. Am. Chem. Soc.*, 2019, **141**, 15755–15760.
14 Y. Li, X. Ma, X. Xu, Y. Ye and B. Wang, *Chem.–Eur. J.*, 2023, **29**, e202203534.
15 T. Zhu, J. Bie, C. Ji, X. Zhang, L. Li, X. Liu, X.-Y. Huang, W. Fa, S. Chen and J. Luo, *Nat. Commun.*, 2022, **13**, 7702.

16 Y. Chen, L. Tang, X. Zeng, W. Guo, T. Yang, H. Xu, Y. Liu, G. Gou, Y. Zhao, J. Luo and Z. Sun, *Adv. Funct. Mater.*, 2024, **34**, 2311726.
17 X. Li, F. Wu, Y. Yao, W. Wu, C. Ji, L. Li, Z. Sun, J. Luo and X. Liu, *J. Am. Chem. Soc.*, 2022, **144**, 14031–14036.
18 W. Guo, H. Xu, F. Sun, Y. Liu, Y. Ma, W. Liu, Y. Zhao, Z. Sun and J. Luo, *Angew. Chem., Int. Ed.*, 2025, **64**, e202421463.
19 G. Yumoto, F. Harata, T. Nakamura, A. Wakamiya and Y. Kanemitsu, *Sci. Adv.*, 2024, **10**, eadq5521.
20 K. Aizu, *Phys. Rev. B*, 1970, **2**, 754–772.
21 K. Tao, C. Xiong, H. Yang, H. Lin, D. Ma, H. Li, S. Lin and B. Wang, *Inorg. Chem. Front.*, 2024, **11**, 5624–5635.
22 S. Wang, X. Liu, L. Li, C. Ji, Z. Sun, Z. Wu, M. Hong and J. Luo, *J. Am. Chem. Soc.*, 2019, **141**, 7693–7697.
23 S. You, Z.-K. Zhu, S. Dai, J. Wu, Q. Guan, T. Zhu, P. Yu, C. Chen, Q. Chen and J. Luo, *Adv. Funct. Mater.*, 2023, **33**, 2303523.
24 R. Gautier, J. M. Klingsporn, R. P. Van Duyne and K. R. Poeppelmeier, *Nat. Mater.*, 2016, **15**, 591–592.
25 K. Claborn, C. Isborn, W. Kaminsky and B. Kahr, *Angew. Chem., Int. Ed.*, 2008, **47**, 5706–5717.
26 W.-Q. Liao, Y.-Y. Tang, P.-F. Li, Y.-M. You and R.-G. Xiong, *J. Am. Chem. Soc.*, 2017, **139**, 18071–18077.
27 K. Aizu, *J. Phys. Soc. Jpn.*, 1969, **27**, 387–396.
28 S. Han, M. Li, Y. Liu, W. Guo, M.-C. Hong, Z. Sun and J. Luo, *Nat. Commun.*, 2021, **12**, 284.
29 S. Han, L. Li, C. Ji, X. Liu, G.-E. Wang, G. Xu, Z. Sun and J. Luo, *J. Am. Chem. Soc.*, 2023, **145**, 12853–12860.
30 P.-F. Li, Y.-Y. Tang, Z.-X. Wang, H.-Y. Ye, Y.-M. You and R.-G. Xiong, *Nat. Commun.*, 2016, **7**, 13635.
31 W.-J. Xu, P.-F. Li, Y.-Y. Tang, W.-X. Zhang, R.-G. Xiong and X.-M. Chen, *J. Am. Chem. Soc.*, 2017, **139**, 6369–6375.
32 Y. C. Kim, K. H. Kim, D.-Y. Son, D.-N. Jeong, J.-Y. Seo, Y. S. Choi, I. T. Han, S. Y. Lee and N.-G. Park, *Nature*, 2017, **550**, 87–91.
33 L. Wang, Y. Xue, M. Cui, Y. Huang, H. Xu, C. Qin, J. Yang, H. Dai and M. Yuan, *Angew. Chem., Int. Ed.*, 2020, **59**, 6442–6450.
34 K. Dong, X. Yang, F. Yao, H. Cong, H. Zhou, S. Zhou, H. Cui, S. Wang, C. Tao, C. Sun, H. Fu, W. Ke and G. Fang, *Adv. Mater.*, 2024, **36**, 2313889.
35 Y. Zhang, D. Wang, W. He, C. Zhao, D. Ling, L. Chen, W. Wu, Q. Geng, X. Fang, G. Liu, L. Zhao and J. Wang, *Chem. Eng. J.*, 2026, **527**, 171989.
36 W. He, L. Kong, P. Yu and G. Yang, *Adv. Mater.*, 2023, **35**, 2209995.
37 C. Liu, R. Wang, J. Liu, W. Xu, H. Zhang, X. Liu, X. Huo, X. Cui, H. Sun, R. Liu, H. Zhu, W. Zhang and J. Ding, *Adv. Opt. Mater.*, 2025, **13**, 2403123.
38 X.-B. Han and W. Zhang, *J. Phys. Chem. Lett.*, 2024, **15**, 5239–5242.
39 X.-B. Han, C.-D. Liu, C.-Q. Jing, M.-L. Jin, W. Wang, J.-M. Zhang, B.-D. Liang and W. Zhang, *J. Phys. Chem. Lett.*, 2025, **16**, 642–649.
40 T. Zhu, W. Weng, C. Ji, X. Zhang, H. Ye, Y. Yao, X. Li, J. Li, W. Lin and J. Luo, *J. Am. Chem. Soc.*, 2022, **144**, 18062–18068.
41 Z. Xu, T. Chen, J. Liang, X. Dong, Y. Geng, L. Li, Z. Sun and J. Luo, *Angew. Chem., Int. Ed.*, 2025, e202513386.
42 Z. Li, C. Ji, Y. Fan, T. Zhu, S. You, J. Wu, R. Li, Z.-K. Zhu, P. Yu, X. Kuang and J. Luo, *J. Am. Chem. Soc.*, 2023, **145**, 25134–25142.
43 Q. Gu, K. Chen, X. Zhang, S. Wang, S. Wu and W. Huang, *ACS Appl. Mater. Interfaces*, 2025, **17**, 17127–17134.
44 H. Chen, J. Lin, J. Kang, Q. Kong, D. Lu, J. Kang, M. Lai, L. N. Quan, Z. Lin, J. Jin, L.-w. Wang, M. F. Toney and P. Yang, *Sci. Adv.*, 2020, **6**, eaay4045.